

# Centimeter-Accuracy Smoothed Vehicle Trajectory Estimation

© PHOTODISC

Anh Vu, Jay A. Farrell, and Matthew Barth

Electrical Engineering Department, University of California, Riverside, CA

E-mails: [anhvu@ee.ucr.edu](mailto:anhvu@ee.ucr.edu),

[farrell@ee.ucr.edu](mailto:farrell@ee.ucr.edu), [barth@ee.ucr.edu](mailto:barth@ee.ucr.edu)

**Abstract**—Next generation roadway maps and vehicle navigation systems have the objective of reliably achieving where-in-lane positioning accuracy. Various methods are under consideration both to attain the requisite roadway map accuracy via post-processing and real-time vehicle positioning accuracy and reliability. Fundamental to these methods is the problem of accurately and reliably estimating a sensor platform trajectory in a post-processing environment. For mapping, the platform trajectory provides the pose for feature sensors (e.g., camera, LIDAR, RADAR). For navigation, the platform trajectory is the ground-truth reference.

This article describes a smoothing framework for estimating sensor platform trajectories using an Inertial Measurement Unit (IMU) and a dual-frequency GPS pseudo-range and carrier-phase

receiver. A Bayesian estimation framework is presented and transformed to a series of nonlinear least squares problems. The result of this optimization process is the platform trajectory estimate at the IMU measurement rate (200 Hz) with position accuracy at the centimeter level. One of the contributions of this research is the method developed to solve for the carrier-phase integer ambiguities. Real-world experimental results are presented to validate the proposed smoothing framework.

## I. Introduction

In Advanced Driver Assistance Systems (ADAS) or Vehicle Assist and Automation (VAA) systems, accurate vehicle positioning is critical, with respect to a digital map representation of the roadway environment [1]. A typical ADAS combines vehicle state with a digital map of the roadway environment to provide the driver with important information [2, 3]; examples include curve-over-safe-speed warning [4], road/lane departure warnings and so forth. Such applications require digital maps with lane-level accuracy

This work was supported in part by the U.S. Department of Transportation—Federal Highway Administration under Grants DTFH61-09-C-00018, and DTFH61-06-D-00006.

Digital Object Identifier 10.1109/MITS.2013.2281009

Date of publication: 25 October 2013

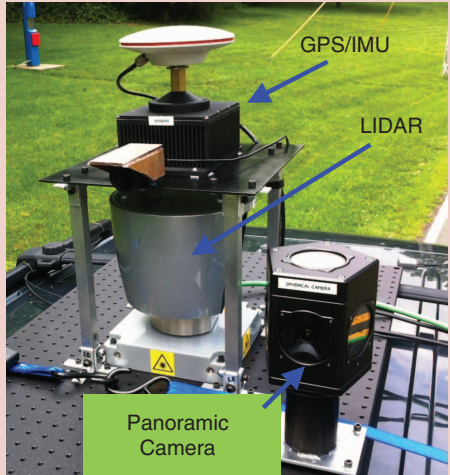


**FIG 1** A typical sensor platform containing a panoramic camera, 3-D LIDAR, a GNSS receiver, and a MEMS IMU.

(pos. error < 0.5 m) and roadway attributes, such as the curvature [3, 5, 6].

The foundation of advanced vehicle control and safety systems is having accurate and reliable knowledge of the current vehicle state vector in real-time. Differential Global Navigation Satellite System (GNSS)-based pseudo-range or carrier-phase aiding of an inertial navigation (or encoder based dead-reckoning) system are the well-known solutions; however, GNSS signal reception can be challenging in urban environments. Feature-based aiding using camera [7–10], RADAR [11], or LIDAR

[12, 13] are feasible additional aiding methods, especially in urban environments. When precise maps of roadway relative features are available, such feature aiding methods can also achieve real-time where-in-lane accuracy [7, 17].

Governmental agencies and various research groups are actively pursuing advanced methods for automated precision mapping of roadway relative features (lane edges, signs, stop lights, street lights, etc.) [12–18]. One common approach is to create large databases of point-cloud features as a map and then later performing vehicle positioning by matching real-time point-cloud features to this map database [12, 13]. Other methods (such as that described in this paper) create maps by extracting key features relative to the earth frame and then later perform positioning by using real-time extracted features to aid on-board inertial measurement units [7–11]. For both approaches, a typical instrumentation package for a roadway survey system is shown in the photograph of Fig. 1.

The LIDAR and camera return data useful for the identification and mapping of roadway relative features in the reference frame of the sensor platform. In an absolute mapping/positioning approach, the map of roadway features is required in the earth frame. Thus, the purpose of the GNSS receiver and IMU is to enable accurate estimation of the pose of the sensor platform relative to the earth frame. Knowledge of the sensor pose and the extrinsic calibration parameters of the LIDAR and camera enable completion of the mapping process by transformation of the roadway features from platform frame to earth frame.

A typical process for development and application of roadway relative maps is depicted in Fig. 2. The map development process is illustrated in the blue boxes of the left column. A set of instruments is mounted on a platform on the mapping vehicle and driven along roadways while acquiring data. These raw data are stored for off-line processing. The offline processing determines the sensor platform trajectory through a process classified as smoothing [19], identifies and classifies objects detected along the roadway, and estimates important attributes (e.g., pose in the ECEF frame) of specific roadway characteristics and features (e.g., sign type and location, stop light type and location, roadway and lane edge curves) along with the sensor extrinsic calibration parameters. The attributes of the roadway relative features are stored in a database and are distributed by various means in support of transportation applications [20]. After the mapping phase is complete, the sensor platform trajectory may be discarded, as it is not in itself part of the

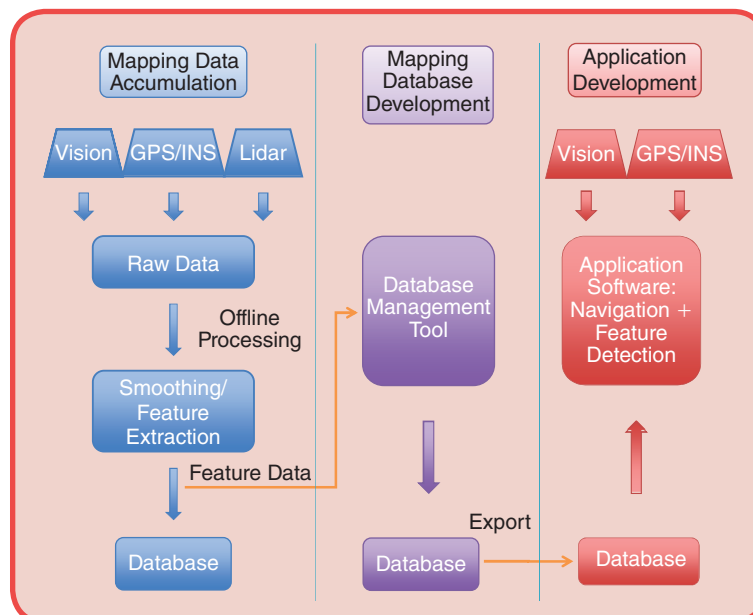


**FIG 2** Roadway map and application development.

roadway map; nonetheless, its accurate estimation is the foundation on which the accuracy of the resulting roadway map is based.

Smoothed vehicle trajectories are also fundamental to the task of real-time vehicle localization, which is classified as filtering [19]. *Smoothing* is a non-causal operation on the data using past ( $\tau < t$ ), present ( $\tau = t$ ) and future ( $\tau > t$ ) measurements  $y(\tau)$  to estimate the platform pose  $x(t)$  at each time  $t$ . *Filtering* is a causal operation using both past and present ( $\tau \leq t$ ) measurements to estimate the platform pose at each time  $t$ . Smoothed trajectories have lower levels of uncertainty and greater accuracy than filtered trajectories; therefore, they can be used to represent ground truth for the error analysis of real-time filtering methods [7–15], SLAM [22, 23] and visual odometry [33].

Post-processing software such as Inertial Explorer [34] uses the Rauch-Tung-Striebel smoother to obtain estimated trajectories during periods when GPS is not available. Dellaert and Kaess' Square Root SAM [21] and Thrun et al.'s GraphSLAM [22] methods solve for both the sensor platform trajectory and the roadway map features, using a Bayesian optimization process built in part on feature-based sensors (e.g. camera(s), RADAR, and LIDAR), without GNSS measurements. The Square Root SAM method estimates both the platform trajectory ( $x(t)$  for all  $t \in [0, T]$ ) and each feature pose jointly. GraphSLAM first marginalizes the feature measurements, and then solves the smaller problem of determining the platform trajectory, finally solving the feature pose estimation problem. It is mentioned in [22] that GPS measurements can be integrated into the GraphSLAM framework, and in [23] the Square Root SLAM method is extended to include Differential GPS (DGPS) pseudo-range measurements. However, quantitative analysis from [21–23] are not sufficient to determine whether these methods can resolve the platform trajectory to centimeter-level accuracy. DGPS pseudo-range measurements are accurate to the 1–2 meter level, while differential carrier-phase measurements are accurate to the centimeter level; however, use of the differential carrier-phase requires resolution of the integer ambiguities.

As an extension of the Square Root SAM method, the platform trajectory estimation method described in this paper uses: 1) raw dual-frequency GPS pseudo-range, Doppler, and carrier-phase measurements, and 2) inertial measurements which include specific force (i.e., acceleration) and angular rates along three perpendicular axes, to obtain platform trajectories with centimeter-level position accuracy. In addition to the overall smoothing procedure, the main novelty of this method comes from the estimation of the GPS carrier-phase integer ambiguities, which is necessary to utilize carrier-phase.

This paper is organized as follows. Section II establishes the notation, sensor frames, and introduces the sensor

measurements. Section III describes the smoothing framework problem statement followed by the description of the smoothing process in Section IV. Real-world experimental results are shown in Section V. Concluding remarks are provided in Section VI.

## II. Sensor Frames and Sensor Measurements

To clearly discuss the sensor processing, various reference frames are required. We use  $\{A\}$  to denote frame  $A$ 's coordinate system. The symbol  ${}^A R$  represents the  $3 \times 3$  rotation matrix for transforming the representation of vectors from frame  $A$  to frame  $B$ . The symbol  ${}^C T_{AB}$  denotes a  $3 \times 1$  vector that points from point  $A$  to point  $B$  and is represented in reference frame  $C$ . The  $3 \times 3$  skew symmetric matrix representation of a vector  $a$  is  $[a \times]$ . The symbol  ${}^A \Omega_{BC} = [{}^A \omega_{BC} \times]$  represents the skew symmetric matrix form of angular rate vector  ${}^A \omega_{BC}$ . Notations with a tilde as an accent character represent measured quantities; notations with a hat as an accent character represent estimated quantities.

### A. Sensor Frames

This paper uses the following three reference frames:

- The Earth-Center, Earth-Fixed (ECEF) frame is denoted by  $\{E\}$ . The origin is at the center of mass of the earth. The axes are the standard WGS definitions.
- The navigation frame is denoted by  $\{N\}$ . The origin is selected at a fixed location convenient for the analysis, for example, the base station antenna. This is a local tangent frame with axes pointing along North, East, and Down (NED) directions.
- The body or platform frame  $\{B\}$  has its origin at the GPS antenna's phase-center. It has its three orthogonal axes defined along the forward (u), right lateral (v), and (w) right-hand orthogonal axes. Inertial measurements along these three axes are the inertial measurements at the origin of  $\{B\}$ . The lever arm distance between the GPS antenna's phase center and the IMU is small enough that it is ignored.

The  $\{E\}$  frame is used as the mapping reference and state estimation frame. The  $\{N\}$  frame is used to present the trajectory and mapping results to humans for visual processing. The platform or body frame  $\{B\}$  is the frame of reference to which the feature sensors, the dual-frequency GPS receiver and an Inertial Measurement Unit (IMU) are rigidly attached. Reference frames are discussed more completely in [24].

For transportation systems, the dominant earth coordinate systems are ECEF rectangular or geodetic and local tangent plane. Transformation between ECEF and geodetic and local tangent frame are straightforward. The methods defined herein could be developed using any of these coordinates systems, and others, with no theoretical differences, but minor implementation changes. Herein,

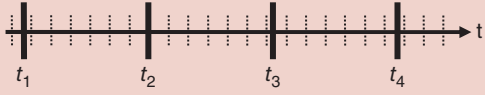


**FIG 3** An illustration of the measurement time where the solid vertical lines represent the time GPS observables are applicable, and the vertical dotted lines represent inertial measurements.

we select the ECEF frame over the local tangent frame for the integration, so that the main system is globally applicable. The transformation to a local frame is only required for the user interface.

### B. Sensor Measurement Timing

The sensor suite consists of a dual-frequency GPS receiver, feature sensors (LIDAR and camera), and an IMU. The GPS and the IMU will be the focus of this paper. The feature sensors will be discussed briefly, to motivate the context of the problem. A key issue is the accurate recording of relative timing information related to the sensor measurements, because for a vehicle moving with velocity  ${}^E\mathbf{v}$ , a timing error  $\delta t$  causes a platform position error of  ${}^E\mathbf{v} \delta t$  and a rotation error  ${}^E\mathbf{\Omega}_{BE} \delta t$ . The GPS receiver is the most accurate timing source in the system and provides a pulse signal once per second (i.e., the 1-PPS signal) aligned with the receiver clock. The GPS receiver clock error can be estimated as a step in the GPS position resolution process. The computer clock marks the arrival of all sensor measurements and the GPS 1-PPS signal. The computer clock drift between 1-PPS signals is small and is neglected.

In Fig. 3, the IMU measurement times are indicated by the vertical dotted lines. The IMU measurements arrive at approximately 200 Hz. The remaining sensors are not synchronized with the IMU, so their measurement times will not align perfectly with the IMU measurement times. The GPS measurement is aligned with the 1-PPS, so that the arrival of the 1-PPS signal allows the GPS measurement to be matched to either the closest IMU measurement time or to be interpolated between two IMU measurement time instants. Similar care is required with the timing of the feature sensors to ensure that their measurements are associated with the most appropriate platform pose.

### C. Inertial Measurement Unit (IMU)

The IMU provides two vector measurements. The  $3 \times 1$  specific force measurement is

$${}^B\tilde{\mathbf{f}} = {}^B\mathbf{a}_{IB} - {}^B\mathbf{g} + \mathbf{b}_a + \mathbf{v}_a, \quad (1)$$

where the subscript  $i$  represents the inertial frame,  ${}^B\mathbf{g} = {}^N\mathbf{R}^N\mathbf{g}$  where  ${}^N\mathbf{g} = [0, 0, g]^T$  is gravity,  ${}^B\mathbf{a}_{IB}$  is the acceleration vector of the platform relative to the inertial

frame,  $\mathbf{v}_a$  represents measurement noise with distribution  $\mathcal{N}(\mathbf{0}, \sigma_a^2 \mathbf{I})$ , and  $\mathbf{b}_a$  is the time-correlated measurement error (i.e. the bias) vector. The  $3 \times 1$  rotation rate measurement is

$${}^B\tilde{\boldsymbol{\omega}}_{IB} = {}^B\boldsymbol{\omega}_{IB} + \mathbf{b}_g + \mathbf{v}_g, \quad (2)$$

where  ${}^B\boldsymbol{\omega}_{IB}$  is the rotation rate vector,  $\mathbf{v}_g$  is the measurement noise with distribution  $\mathcal{N}(\mathbf{0}, \sigma_g^2 \mathbf{I})$ , and  $\mathbf{b}_g$  is the gyro bias vector. The biases are modeled as vector Gauss-Markov processes

$$\begin{aligned} \delta\dot{\mathbf{b}}_a &= -\lambda_a \delta\mathbf{b}_a + \mathbf{v}_{ba}, \quad \mathbf{v}_{ba} \sim \mathcal{N}(\mathbf{0}, \sigma_{ba}^2 \mathbf{I}) \quad \text{and} \\ \delta\dot{\mathbf{b}}_g &= -\lambda_g \delta\mathbf{b}_g + \mathbf{v}_{bg}, \quad \mathbf{v}_{bg} \sim \mathcal{N}(\mathbf{0}, \sigma_{bg}^2 \mathbf{I}). \end{aligned} \quad (3)$$

The biases and additional IMU calibration parameters can be estimated in the smoothing process.

### D. Feature Sensors

Feature sensors include camera, LIDAR, and RADAR. Such sensors measure the intensity of received electromagnetic energy either reflected or emitted by objects in their environment. The received signals are processed by various means to detect objects-of-interest (e.g. [7,15, 25–28,33]). For such objects, the processed data from each of these sensors can provide the equivalent of the angle from the sensor to the object, in the sensor frame of reference. In addition, LIDAR and RADAR provide the range from the sensor to the object. Such feature-based angle and range measurements are in the sensor frame that is valid at the time of the measurement. This frame is a non-inertial frame that is rigidly attached to the moving sensor platform. The extrinsic sensor parameters define the pose (translation and attitude) of the sensor with respect to the platform. The extrinsic parameters are accurately calibrated both a priori and during the feature map extraction process.

The measured returns from feature sensors will be generically referred to as images. Feature sensors return a sequence of images. Objects are detected in each image by their features, which are tracked and associated with the similar features in past and future images. This sequence of feature detections, if obtained from a sufficiently diverse set of vehicle poses, enables accurate mapping of the object location in post-processing. The objectives of the feature detection, tracking, and association sub-tasks are greatly facilitated when an accurate estimate of the sensor platform trajectory is available. Provision of such a trajectory estimate is the objective of the procedure described herein.

### E. GPS Measurements

The GPS receiver provides carrier-phase, Doppler, and pseudo-range measurements, as well as signal quality indicators, for both L1 and L2. These observables are

recorded at 1 Hz and are applicable at the beginning of the second indicated by a 1-PPS signal from the GPS receiver.

The pseudo-range measurement model is

$$\rho_1^i = \rho^i + c\Delta t^i + \frac{f_2}{f_1} I_r^i + \chi^i + M_{\rho 1}^i + \eta_{\rho 1}^i \quad (4)$$

$$\tilde{\rho}_2^i = \rho^i + c\Delta t^i + \frac{f_1}{f_2} I_r^i + \chi^i + M_{\rho 2}^i + \eta_{\rho 2}^i, \quad (5)$$

where  $f_1$  and  $f_2$  are the carrier frequencies of the L1 and L2 signals and

$$\rho^i = \|\mathbf{p} - \mathbf{p}_{sv}^i\| + c\Delta t_r \quad (6)$$

denotes the pseudo-range between the  $i$ th satellite vehicle and the origin of the  $B$  frame at the measurement time,  $\mathbf{p}_{sv}^i$  is the position of the antenna of the  $i$ th satellite vehicle, and  $\Delta t_r$  is the receiver clock bias. The receiver antenna's phase center (origin of the  $B$  frame) is represented as  $\mathbf{p}$ . The symbols  $\tilde{\rho}_1$  and  $\tilde{\rho}_2$  will represent the vector of pseudo-range measurements at each frequency.

The common mode errors present in the pseudo-range and carrier-phase measurements are represented by  $\{\Delta t^i, I_r^i, \chi^i\}$ , which consist of the satellite clock error, the atmosphere errors, and the ephemeris error. These common mode errors can be removed by differential corrections (single differencing). The receiver clock bias  $\Delta t_r$  can either be estimated or removed using double differencing (Section 8.8.5 in [24]).

The carrier-phase measurement model is

$$\lambda_1 \tilde{\phi}_1^i = \rho^i + c\Delta t^i - \frac{f_2}{f_1} I_r^i + \chi^i + M_{\phi 1}^i + N_1^i \lambda_1 + \eta_{\phi 1}^i \quad (7)$$

$$\lambda_2 \tilde{\phi}_2^i = \rho^i + c\Delta t^i - \frac{f_1}{f_2} I_r^i + \chi^i + M_{\phi 2}^i + N_2^i \lambda_2 + \eta_{\phi 2}^i, \quad (8)$$

where  $M_{\{\rho, \phi\}x}^i$  represents multipath errors in pseudo-range and carrier-phase measurements while  $\eta_{\{\rho, D, \phi\}x}^i$  represents the noise in the measurements. The multipath effects on the pseudo-range are at the meter level, while on the carrier-phase it is at the centimeter level. The noise effects on the pseudo-range are at the decimeter level, while on the carrier-phase it is at the millimeter level. The symbols  $N_1^i$  and  $N_2^i$  represent an unknown integer ambiguities, which are constant during time intervals when the receiver phase-locked-loop maintains phase-lock to the satellite. The integer ambiguities are multiplied by the corresponding wavelengths  $\lambda_{\{1,2\}}$ . When this integer ambiguity vectors can be correctly identified, the integer ambiguity corrected phase measurement provides a measure accurate to the centimeter level. The symbols  $\tilde{\phi}_1$  and  $\tilde{\phi}_2$  will represent the vectors of carrier-phase measurements. The symbol  $\mathbf{R}_k$  represents the measurement noise covariance matrix at  $t_k$  for the vector of GPS measurements.

The Doppler measurement model is

$$\lambda_1 \tilde{D}_1^i = \tilde{\mathbf{I}}_{ir}^T (\mathbf{v} - \mathbf{v}_{sv}^i) + c\Delta t_r - c\Delta t^i + \eta_{D1}^i \quad (9)$$

$$\lambda_2 \tilde{D}_2^i = \tilde{\mathbf{I}}_{ir}^T (\mathbf{v} - \mathbf{v}_{sv}^i) + c\Delta t_r - c\Delta t^i + \eta_{D2}^i, \quad (10)$$

where time derivatives of the common mode errors are small and have been neglected and  $\tilde{\mathbf{I}}_{ir}^T = [\mathbf{p} - \mathbf{p}_{sv}^i / \|\mathbf{p} - \mathbf{p}_{sv}^i\|]^T$  is the unit vector pointing from the  $i$ th satellite vehicle to the GPS receiver antenna.

### III. Smoothing Problem Statement

The platform kinematic model has the form

$${}^E \dot{\mathbf{x}} = \mathbf{f}(\mathbf{x}, \mathbf{u}). \quad (11)$$

The rover or platform (refers to the origin of the  $B$  frame) state vector is defined as:

$$\mathbf{x} = [{}^E \mathbf{p}^T, {}^E \mathbf{v}^T, {}^E \boldsymbol{\Theta}^T, \mathbf{b}_a^T, \mathbf{b}_g^T]^T, \quad (12)$$

where  ${}^E \mathbf{p} = [{}^E x, {}^E y, {}^E z]^T$ ,  ${}^E \mathbf{v} = [{}^E v_x, {}^E v_y, {}^E v_z]^T$ ,  ${}^E \boldsymbol{\Theta} = [\phi, \theta, \psi]^T$  (roll, pitch, yaw) are the position, velocity, and orientation relative to the  $E$  frame, and  $\{\mathbf{b}_a, \mathbf{b}_g\}$  are the accelerometer and gyro biases represented in the body frame. We are given two sets of measurements:

$$\tilde{\mathbf{y}} = \{[\tilde{\rho}_1(t_k) \ \tilde{\rho}_2(t_k) \ \tilde{\phi}_1(t_k) \ \tilde{\phi}_2(t_k)]\}$$

$$\tilde{\mathbf{u}} = \{{}^B \tilde{\mathbf{f}}(\tau_j) \ {}^B \tilde{\boldsymbol{\omega}}_{IB}(\tau_j)\}, \quad (13)$$

where  $t_k = i$  for  $i = 1, \dots, M$  represent the 1 Hz GPS measurement times and  $\tau_j = 0.005j$  for  $j = 1, \dots, M_{200}$  represent the 200 Hz IMU measurement times.

The Doppler measurement noise is typically at the cm/s level. The Doppler measurement is derived from the same information as the carrier-phase measurement; therefore, only one or the other measurement should be used in any epoch. The experimental results will also use Doppler measurements in the smoothing process, at times when carrier-phase integer ambiguities are not known. We do not discuss the Doppler measurements in the presentation of the smoothing process for succinctness. The extension to include Doppler measurements is straightforward.

The solution of eqn. (11) over the interval  $t \in [t_{k-1}, t_k]$  from the initial condition,  $\mathbf{x}_{k-1}$ , is denoted as  $\Phi(\mathbf{x}_{k-1}, \mathbf{u}_{k-1})$  where  $\mathbf{u}_{k-1}$  is the subset of  $\tilde{\mathbf{u}}$  containing measurements in this time interval. The mapping

$$\Phi(\mathbf{x}_{k-1}, \mathbf{u}_{k-1}) = \mathbf{x}_{k-1} + \int_{t_{k-1}}^{t_k} \mathbf{f}(\mathbf{x}(\tau), \mathbf{u}(\tau)) d\tau \quad (14)$$

predicts the value of the next state  $\mathbf{x}_k$ . The linearized version of this operator predicts the propagation of the error state:

$$\delta \mathbf{x}_k = \Phi_{k-1} \delta \mathbf{x}_{k-1} + \mathbf{w}_{k-1}, \quad (15)$$

where  $\mathbf{Qd}_k = \text{cov}(\mathbf{w}_k)$  is the covariance of the discrete-time process noise  $\mathbf{w}_k$  and  $\Phi_{k-1}$  is the linearization of  $\Phi(\mathbf{x}_{k-1}, \mathbf{u}_{k-1})$  over the time interval  $t \in [t_{k-1}, t_k]$ . Computation of  $\mathbf{Qd}_k$  and  $\Phi_{k-1}$  is discussed in Section 7.2.5.2 of [24].

The objective of the smoothing process is to estimate the state vector trajectory over the entire run. It is sufficient to define the cost function using only the state vector at each of the time instants  $t_k$  at which the GPS observables are applicable:

$$\mathbf{x}_{1:M} = [\mathbf{x}_1^T, \mathbf{x}_2^T, \dots, \mathbf{x}_{M-1}^T, \mathbf{x}_M^T]^T. \quad (16)$$

The optimal state estimate at the higher rate of the IMU, between any two of the GPS measurement time instants, can be computed by interpolation between the forward and backward integrals of eqn. (11) over the one-second interval.

Optimality is defined by the degree of consistency with both sets of measurements, interpreted in the Bayesian sense, as a maximum likelihood estimator over the available measurement data with the objective function defined by the state constraint distributions [21]:

$$p(\mathbf{x}_k | \mathbf{x}_{k-1}, \mathbf{u}_{k-1}) \propto \exp\left(-\frac{1}{2}(\mathbf{x}_k - \Phi(\mathbf{x}_{k-1}, \mathbf{u}_{k-1}))^T \mathbf{Qd}_k^{-1} (\mathbf{x}_k - \Phi(\mathbf{x}_{k-1}, \mathbf{u}_{k-1}))\right) \quad (17)$$

and the measurement constraint distributions:

$$p(\mathbf{y}_k | \mathbf{x}_k) \propto \exp\left(-\frac{1}{2}(\tilde{\mathbf{y}}_k - \mathbf{y}_k(\mathbf{x}_k))^T \mathbf{R}_k^{-1} (\tilde{\mathbf{y}}_k - \mathbf{y}_k(\mathbf{x}_k))\right). \quad (18)$$

The maximum likelihood estimate is

$$\hat{\mathbf{x}}_{1:M} = \arg \max_x \left( \prod_{k=1}^M p(\mathbf{x}_k | \mathbf{x}_{k-1}, \mathbf{u}_{k-1}) p(\mathbf{y}_k | \mathbf{x}_k) \right). \quad (19)$$

Working with the log-likelihood transforms the smoothing problem to the task of choosing the trajectory  $\mathbf{x}$  to minimize

$$S(\mathbf{x}_{1:M}) = \sum_{k=1}^M (\|\mathbf{x}_k - \Phi(\mathbf{x}_{k-1}, \mathbf{u}_{k-1})\|_{Qd_k}^2 + \|\tilde{\mathbf{y}}_k - \mathbf{y}_k(\mathbf{x}_k)\|_{R_k}^2), \quad (20)$$

which is solved numerically. Implementation of this process requires specification of the required partial derivative matrices and definition of the method to estimate the integer ambiguities.

#### IV. Smoothing Framework

This section describes the smoothing framework. The subsections describe the platform kinematic model, summarize the error state model, describe the optimization procedure, and the method used to resolve the carrier-phase integer ambiguity. The presentation herein is succinct. Additional details can be found in Chapter 11 in [24].

##### A. Mechanization Equations

The kinematic model of eqn. (11) is:

$${}^E\dot{\mathbf{p}} = {}^E\hat{\mathbf{v}} \quad (21)$$

$${}^E\dot{\mathbf{v}} = {}^E_B\hat{\mathbf{R}} {}^B\hat{\mathbf{f}} + {}^E_N\mathbf{R}^N \mathbf{g} - 2{}^E\Omega_{iE} {}^E\hat{\mathbf{v}} \quad (22)$$

$${}^E\dot{\Theta} = {}^E_B\hat{\Omega} (-{}^E_B\hat{\mathbf{R}} {}^E\omega_{iE} + {}^E\hat{\omega}_{iB}), \quad (23)$$

where  $\hat{\mathbf{u}} = [{}^B\hat{\mathbf{f}}^T, {}^E\hat{\omega}_{iB}^T]^T$ ,  ${}^B\hat{\mathbf{f}} = {}^B\tilde{\mathbf{f}} - \hat{b}_a$ ,  ${}^E\hat{\omega}_{iB} = {}^E\tilde{\omega}_{iB} - \hat{b}_g$ , and

$${}^E_B\hat{\Omega} = \begin{bmatrix} 1 & s_{\phi}t_{\phi} & c_{\phi}t_{\phi} \\ 0 & c_{\phi} & -s_{\phi} \\ 0 & s_{\phi}/c_{\phi} & c_{\phi}/s_{\phi} \end{bmatrix},$$

where  $s_x, c_x$  and  $t_x$  represent the sine, cosine and tangent of the quantity  $x$ .

##### B. Error State Model

The error state vector at time  $t$  is defined as:

$$\delta\mathbf{x} = [\delta^E\mathbf{p}^T, \delta^E\mathbf{v}^T, \delta^E\Theta^T, \delta\mathbf{b}_a^T, \delta\mathbf{b}_g^T]^T, \quad (24)$$

where  $\delta\mathbf{x} = \mathbf{x} - \hat{\mathbf{x}}$ . Using the Taylor series expansion to first order, the dynamic error model is:

$$\delta\dot{\mathbf{x}} = \mathbf{F}\delta\mathbf{x} + \mathbf{G}\omega,$$

where

$$\omega = [\mathbf{v}_a^T, \mathbf{v}_g^T, \mathbf{v}_{ba}^T, \mathbf{v}_{bg}^T]^T, \quad (25)$$

$$\mathbf{F} = \begin{bmatrix} \mathbf{0} & \mathbf{I} & \mathbf{0} & \mathbf{0} & \mathbf{0} \\ \mathbf{F}_{vp} & -2{}^E\Omega_{iE} & \mathbf{F}_{v\Theta} & -{}^E_B\hat{\mathbf{R}} & \mathbf{0} \\ \mathbf{0} & \mathbf{0} & \mathbf{F}_{\Theta\Theta} & \mathbf{0} & -{}^E_B\hat{\Omega} \\ \mathbf{0} & \mathbf{0} & \mathbf{0} & -\lambda_a \mathbf{I} & \mathbf{0} \\ \mathbf{0} & \mathbf{0} & \mathbf{0} & \mathbf{0} & -\lambda_g \mathbf{I} \end{bmatrix}, \quad (26)$$

$$\mathbf{G} = \begin{bmatrix} \mathbf{0} & \mathbf{0} & \mathbf{0} & \mathbf{0} \\ {}^E_B\hat{\mathbf{R}} & \mathbf{0} & \mathbf{0} & \mathbf{0} \\ \mathbf{0} & {}^E_B\hat{\Omega} & \mathbf{0} & \mathbf{0} \\ \mathbf{0} & \mathbf{0} & \mathbf{I} & \mathbf{0} \\ \mathbf{0} & \mathbf{0} & \mathbf{0} & \mathbf{I} \end{bmatrix}. \quad (27)$$

In (26),  $\mathbf{F}_{xy}$  represents the partial derivative of the  $x$ -equation to with respect to  $y$ .

##### C. Optimization

The optimization process has the following steps:

###### 1) Initialization

Theoretically, the initial trajectory can be arbitrary, but accurate initialization decreases the number of iterations required for convergence. For the results shown herein,  $\mathbf{x}_{1:M}$  is initialized using the real-time DGPS-aided Inertial Navigation System (INS) trajectory estimated by the Extended Kalman Filter (EKF) technique described in [7].

## 2) Iterative Numeric Processing

The optimal trajectory  $\mathbf{x}_{1:M}$  can be computed iteratively as the nonlinear weighted least squares problem as shown in [21]. The objective function is  $S(\mathbf{x}_{1:M}) = \mathbf{r}(\mathbf{x}_{1:M})^T \mathbf{P} \mathbf{r}(\mathbf{x}_{1:M})$  where

$$\mathbf{r}(\mathbf{x}_{1:M}) = \begin{bmatrix} \mathbf{x}_2 - \mathbf{f}(\mathbf{x}_1, \hat{\mathbf{u}}_1) \\ \mathbf{x}_3 - \mathbf{f}(\mathbf{x}_2, \hat{\mathbf{u}}_2) \\ \vdots \\ \mathbf{x}_M - \mathbf{f}(\mathbf{x}_{M-1}, \hat{\mathbf{u}}_{M-1}) \\ \tilde{\mathbf{y}}_1 - \hat{\mathbf{y}}_1(\mathbf{x}_1) \\ \tilde{\mathbf{y}}_2 - \hat{\mathbf{y}}_2(\mathbf{x}_2) \\ \vdots \\ \tilde{\mathbf{y}}_M - \hat{\mathbf{y}}_M(\mathbf{x}_M) \end{bmatrix} \text{ and } \mathbf{P} = \text{diag} \begin{bmatrix} \mathbf{Qd}_1 \\ \mathbf{Qd}_2 \\ \vdots \\ \mathbf{Qd}_{M-1} \\ \mathbf{R}_1 \\ \mathbf{R}_2 \\ \vdots \\ \mathbf{R}_M \end{bmatrix}. \quad (28)$$

The matrix  $\mathbf{P}$  is positive definite with a positive definite square root  $\mathbf{W}$  such that  $\mathbf{P} = \mathbf{W}^T \mathbf{W}$ . At each of the iterations, the error state vector  $\delta\mathbf{x}_{1:M}$  is found as the solution of a linear set of equations. To first order, the correction  $\delta\mathbf{x}_{1:M}$  that minimizes  $S(\mathbf{x}_{1:M} + \delta\mathbf{x}_{1:M})$  solves

$$\mathbf{A} \cdot \delta\mathbf{x}_{1:M} = \mathbf{b}, \quad (29)$$

where  $\mathbf{b} = \mathbf{W} \cdot \mathbf{r}$ ,  $\mathbf{A} = \mathbf{W} \cdot \mathbf{J}$ , and

$$\mathbf{J}(\mathbf{x}_{1:M}) = \frac{\partial \mathbf{r}}{\partial \mathbf{x}_{1:M}} = \begin{bmatrix} \Phi_1 & -\mathbf{I} & & & \\ \Phi_2 & -\mathbf{I} & & & \\ \vdots & \ddots & \ddots & & \\ & & & \Phi_{M-1} & -\mathbf{I} \\ \mathbf{H}_1 & & & & \\ \mathbf{H}_2 & & & & \\ \vdots & & & & \\ & & & & \mathbf{H}_M \end{bmatrix}.$$

The matrix  $\mathbf{A}$  is sparse. It incorporates the transition matrices  $\Phi_k$  (transition from  $t_k$  to  $t_{k+1}$ ) and linearized GPS measurement matrices  $\mathbf{H}_k$  using double differences.

## 3) Termination Conditions

The weighted least squares iterations continue until one of these conditions is met: 1) the norm of  $\delta\mathbf{x}_{1:M}$  is below a threshold set as  $\tau_1$  or 2) the ceiling iteration threshold set as  $\tau_2$  has been reached. At the conclusion of the iterative optimization, the error covariance matrix for  $\mathbf{x}_{1:M}$  and  $\delta\mathbf{x}_{1:M}$  is

$$\mathbf{C} = (\mathbf{A}^T \cdot \mathbf{A})^{-1}. \quad (30)$$

## Discussion

The error vector  $\delta\mathbf{x}_{1:M}$  contains corrections  $\delta\mathbf{x}_i$  to the state  $\mathbf{x}_i$  for each time step  $t_i$ . While the incorporation of the correction  $\delta\mathbf{x}_i$  at each iteration is casually indicated as  $\mathbf{x}_i^+ = \mathbf{x}_i^- + \delta\mathbf{x}_i$ . This correction does not apply to the rotation portion of the correction. The angle correction is discussed in eqn. (10.29) in [24]. Also, it is important to notice

that after the first nonlinear least squares correction,  $\mathbf{x}_i^+$  will no longer exactly satisfy eqn. (11), as the cost function defining the maximum likelihood trajectory estimate involves a tradeoff between the kinematic model and the measurement model.

## D. Resolving Carrier-Phase Integer Ambiguity

The carrier-phase measurements from the GPS receiver's phase-locked loop (PLL) can be used as range measurements only after the integer ambiguity in these measurements has been resolved. The origin of the integer ambiguities within the PLL is discussed in Section 8.4.9 of [24]. Once the integer ambiguities are resolved, the integer-resolved phase measurement has multipath and noise at the centimeter and millimeter levels, respectively.

This subsection outlines the vital steps needed to resolve the integer ambiguities in the carrier-phase measurements. The raw GPS measurements are processed through a number of steps, including segmentation of the trajectory into smaller intervals each containing multiple GPS epochs, processing each of the intervals to resolve the integers, integer validation, and extending integers from time intervals with solution to adjacent intervals without integer solutions. A prior full state vector  $\mathbf{x}_{1:M}$  and its covariance matrix  $\mathbf{C}$  is assumed to have been obtained from the batch optimization process using pseudo-range and Doppler measurements.

### 1) Segmentation and Candidate Detection

The carrier-phase measurements from both L1 and L2 along with the lock-time for each of the frequencies are reported for each pseudo-random noise (PRN) code (i.e., satellite vehicle identifier) returned by the GPS receiver. The lock-time for each of the frequencies reported for each PRN increases while the PLL indicates that it has maintained lock in consecutive epochs. Time segments with monotonically increasing lock-time counters are each labeled with a unique integer. The purpose of this step is to find candidate time intervals with at least five PRNs each with satellite elevation above a threshold criteria  $\tau_3$ , each maintaining PLL lock on both L1 and L2. This time segmentation proceeds from  $t_1$  to  $t_M$  to find intervals with consecutive epoch duration between three to ten seconds that meet the above criteria. The three seconds minimum duration lower bound is related to the fact that using data from multiple measurement epochs increases the chance of getting the right integers. The maximum duration of ten seconds provides opportunities for comparing independent integer solutions, because phase lock is typically maintained for significantly longer than ten seconds. Increasing the number of trials allows us to set a smaller threshold in the integer validation step to reject incorrect integer estimates that may occur due to multi-path errors and cycle slips.

## 2) Resolving Integers

For each time segment  $\mathbf{x}_{a:b}$  where  $1 \leq a < b \leq M$ , initial integers  $\mathbf{N} = \begin{bmatrix} N_{L1} \\ N_{L2} \end{bmatrix}$  (this is a vector of integers for valid PRNs in the segment containing both L1 and L2 integers) are computed from the corresponding carrier-phase observables and the previously computed smoothed trajectory using GPS pseudo-range and Doppler measurements. The integers computed are very close to the solution, thus the goal of this step is to estimate the error of the integer vector  $\delta\mathbf{N}$ . The estimation approach is similar to the batch optimization trajectory estimation step described in Section IV.C, yet requires modification since a portion of the vector to be estimated is constrained to be integer. A linear system of equations is formed using this time segment's states, the state transition constraints, and single difference carrier-phase measurements where  $\delta\mathbf{N}$  is augmented to the full state vector. The receiver clock bias (modeled in (6)) from each of the epochs within the time segment is also augmented into the state vector  $\mathbf{x}_{a:b}$  since these quantities have to be estimated in the single difference GPS measurements (discussed in Chapter 8 of [24]). The system of equations has the form

$$\mathbf{A} \cdot \delta\mathbf{x}_{a:b} + \mathbf{B} \cdot \delta\mathbf{N} = \begin{bmatrix} \Phi \\ \mathbf{H} \end{bmatrix} \cdot \delta\mathbf{x}_{a:b} + \begin{bmatrix} \mathbf{0} \\ \mathbf{L} \end{bmatrix} \cdot \delta\mathbf{N} = \mathbf{b}, \quad (31)$$

where  $\mathbf{A}$  (represented by the concatenation of a sparse state transition constraints block  $\Phi$  and a sparse GPS measurement matrix block  $\mathbf{H}$ , which also accounts for the receiver clock biases) and  $\mathbf{b}$  have similar structure to (29), the measurement vector  $\tilde{\mathbf{y}}$  contains carrier-phase phase-range measurements, and  $\mathbf{B} = \begin{bmatrix} \mathbf{0} \\ \mathbf{L} \end{bmatrix}$  accounts for the linearization with respect to the integer error where  $\mathbf{L}$  is a sparse matrix filled with the wavelength values for  $f_1$  and  $f_2$ . Equation (31) separates the full augmented state vector into  $\delta\mathbf{x}_{a:b}$  (a real vector) and  $\delta\mathbf{N}$  (an integer vector).

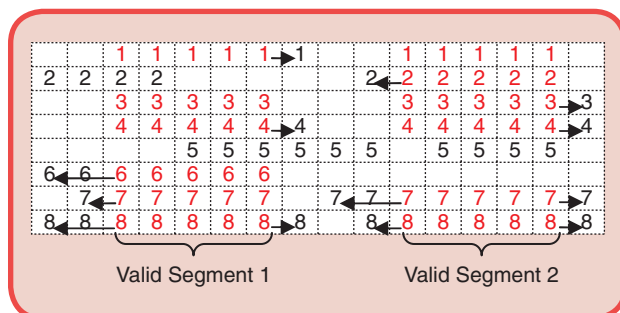


**FIG 4** An example of integer extension for one frequency with 8 PRNs (number 1–8) over 16 epochs of GPS measurements where cells with numbers indicate the PRN codes and PLL lock of the PRN at the second. Consecutive red cells indicate valid segments with resolved integer and arrows indicate extended integers. The minimum segment search is 5 epochs.

Using the MILES method [29] and [30] to deconstruct the problem into one that first solves for the integer vector  $\delta\mathbf{N}$ , then solves for the real vector  $\delta\mathbf{x}_{a:b}$ , then corrects the prior integer estimate by adding  $\delta\mathbf{N}$  to  $\mathbf{N}$ . Solution of the integer least squares problem requires search over the integer vectors within an ellipsoid that shrinks in size as the iteration continues.

## 3) Integer Validation

For each of the segments, the difference between the L1 and L2 phase-ranges

$$res12_k^i = \lambda_1(\tilde{\phi}_1^i(t_k) - N_{L1}^i) - \lambda_2(\tilde{\phi}_2^i(t_k) - N_{L2}^i) \quad (32)$$

is computed over each epoch ( $t_k$ ) and each of the PRNs ( $i$ ) with resolved integers. These values are stored in a list.

Because any constant added to the residual vector at any time is impossible to discriminate from receiver clock error, the median value of the elements of the residual vector is subtracted from each element of that vector. If there are at least five PRNs with  $res12s$  equal to or smaller than  $\tau_4$ , the integers corresponding to those PRNs that pass the check are set as the integers for the candidate segment and the segment is approved as valid.

## 1) Extending Integers

Starting from  $t_1$ , valid segments are identified sequentially in ascending order and the PRNs with integers first extended back in time until the lock is invalid, or the time the previous valid segment's forward pass has been reached. The forward pass extends the PRNs with integers forward in time until  $t_M$  has been reached, or the time the next valid segment has been reached. In addition, individual PRNs are removed from the valid PRN list being extended forward or backward if it fails the  $res12$  check at the extending time. These checks ensure that the PRNs are extended correctly and cycle slips in the PLL are detected. An example is illustrated in Fig. 4.

## V. Experimental Results

This section presents results from using the methods described herein with application to a dataset in which a vehicle collects raw sensor measurements while being driven around the UC-Riverside main campus loop shown in Fig. 5. The smoothing process parameters  $\{\tau_1, \tau_2, \tau_3, \tau_4\}$  are set to  $\{1e-5, 20, 15^\circ, 0.02 \text{ m}\}$ , respectively. Note that the 2 cm threshold for  $\tau_4$  is a very tight constraint. The first smoothing iteration uses IMU, GPS pseudo-range and GPS Doppler measurements resulting in an estimated position state vectors having standard deviations as computed by eqn. (30) at the 0.5 meter level along the North-East plane and 1 meter level along the Down direction. Using this initial smoothed platform trajectory and its covariance matrix sequence as a priori information, candidate segments with

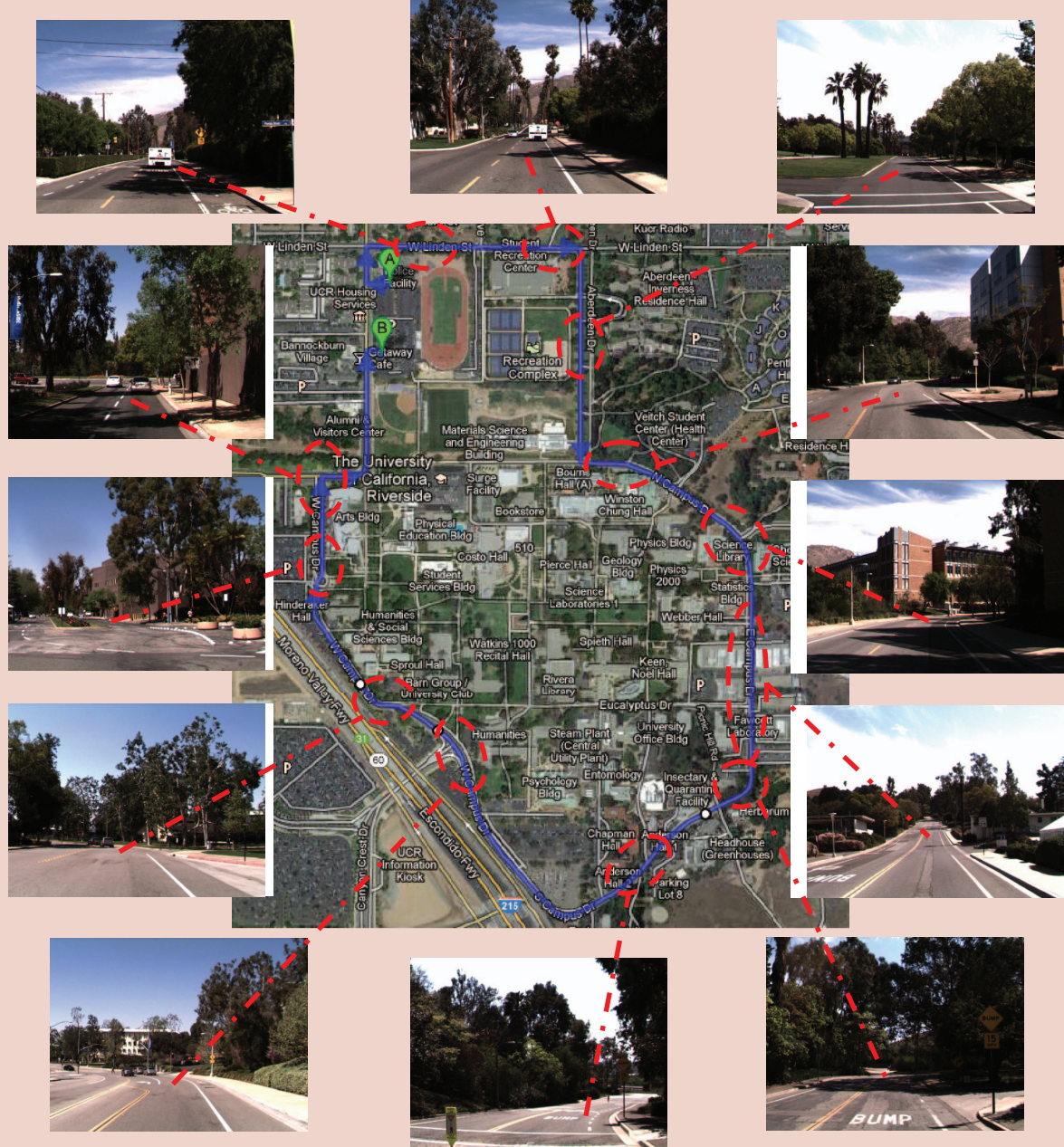


**FIG 5** Map with an overlay of the route taken (in blue) to collect data while driving around UC-Riverside's main campus (satellite image from Google Maps). The trajectory is in the clockwise direction from A to B. Images around the route map show examples of the kind of environment surrounding the path.

resolved integers for carrier-phase measurements are extracted. The segments with valid integers are backward/forward extended into adjacent time intervals without integers according to the integer-extending step. A second smoothing phase uses carrier-phase measurements with valid integer quantities when available and pseudo-range/Doppler measurements when the integer-resolved carrier-phase measurements are not available.

The GPS receiver utilized in the experimental setup is a NovAtel OEMV2 model returning raw measurements tightly coupled with the NV-IMU1000 Microelectromechanical system (MEMS) IMU from NAV Technology Ltd. that returns the specific forces and angular rate measurements along the three orthogonal axes at 200 Hz. From the IMU's specification sheet, the gyroscope has an in run bias stability smaller than 72 degrees/hour and the accelerometer has an in run

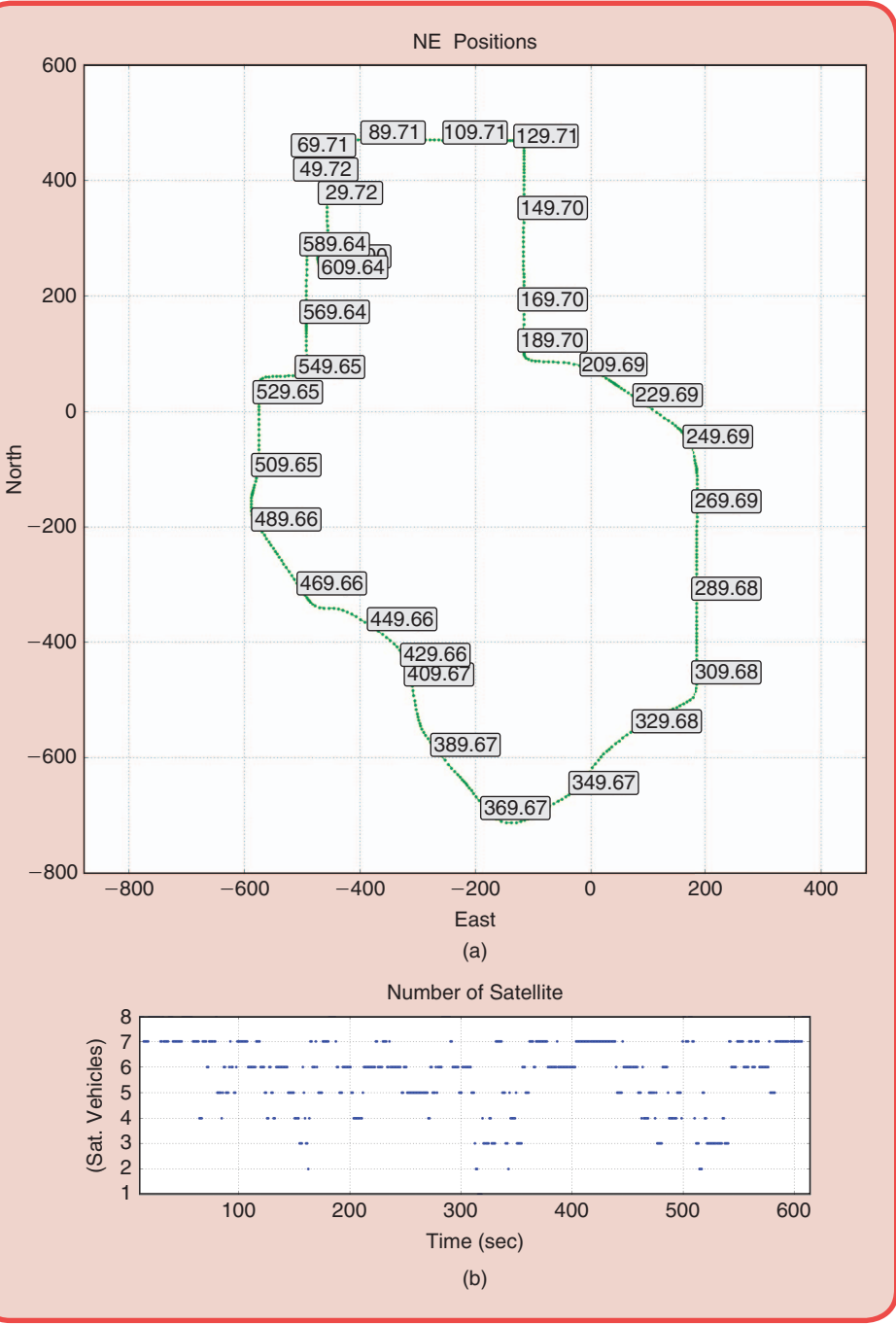


**FIG 6** First plot (a) is a North-East plot of the estimated trajectory along with the approximate time along the route. The time can be used to match up with the environment found in Fig. 5 and the subsequent graphs to enable a thorough analysis. The second plot (b) is the number of visible satellite vehicles with elevation above or equal to  $\tau_3$ .

bias stability smaller than 10 mg, see <http://www.nav.cn/en/>. Running on an Intel i7 (2920XM) with 16 GB of random access memory, the method described in the paper is implemented as a single threaded program in the Python programming language. The entire processing time for the dataset described in this section takes approximately 30 minutes. Additional

speedup can be achieved with a more optimized implementation in C/C++ with parallel numeric processing algorithms.

#### A. Dataset Description

The 3.6 km trip, as shown on the map in Fig. 5, took approximately 600 seconds. The times along the route in seconds is indicated in Fig. 6(a). The vehicle starts out in a parking lot near the northwest corner and returns to the same parking lot after completing the route around the UC-Riverside main campus. The images surrounding the route map in Fig. 5 illustrate the characteristics of the environment found around the trajectory. Foliage and buildings are often present on both sides of the road. This creates substantial challenges for GPS reception. The number of satellite vehicles visible by the GPS antenna with clear line-of-sight is often reduced below four in parts of the dataset due to occlusions from the environment along the route (see Fig. 6(b) for the number of available satellite vehicles versus time). This dataset is a good representation to illustrate the kind of challenges present in suburban to urban environments where GPS reception is intermittent. It also demonstrates the ability of smoothing methods to deal with these environmental challenges. The following subsection provides

an analysis of the smoothing process applied to this dataset with illustrations and graphs.

#### B. Discussion

The plot in Fig. 6(a) shows the final estimated position trajectory transformed into the local North-East position

reference where the time along the route is indicated along the trajectory. The indicated time along the route can be used to match to the time axes in Figs. 5, 6(b), 7, 8, and 9.

The standard deviation plots in NED at the end of the first smoothing stage and at the end of the second smoothing stage are shown in Fig. 8(a) and 8(b) respectively. When matched to the time tags in Fig. 6(a) to perform lookup in Fig. 5, the uncertainty grows in those locations with tall trees and buildings either occlude the GPS antenna's view of the sky or affect the size of the errors in the measurements. Despite the occlusions, the smoothing process using integer-resolved carrier measurements achieves uncertainty at the centimeter-level along the horizontal plane (North-East) the majority of the time as shown in Fig. 8(b). The time intervals over which the carrier-phase measurements are not available can be seen clearly in the carrier-phase residual plots of Fig. 9(b) (160–170 sec., 310–350 sec., and 505–555 sec.). These intervals correspond well to the intervals in Fig. 6b where the number of satellite vehicles with line-of-sight has dropped well below four satellites. While the uncertainty grows during these time intervals, the growth in the uncertainty is slow and only increases to near 0.2 meter. Inclusion of roadway features using methods such as those described in [21, 22, 33], in combination with the integer-resolved carrier-phase as discussed herein, would contain the ECEF resolved platform trajectory and feature location errors to the centimeter level throughout such runs, as is required for lane-level map production.

The residual plots (subsets within  $\mathbf{r}(\mathbf{x}_{1:M})$ ) and the histograms of the blue residual plots are shown in Fig. 9. The

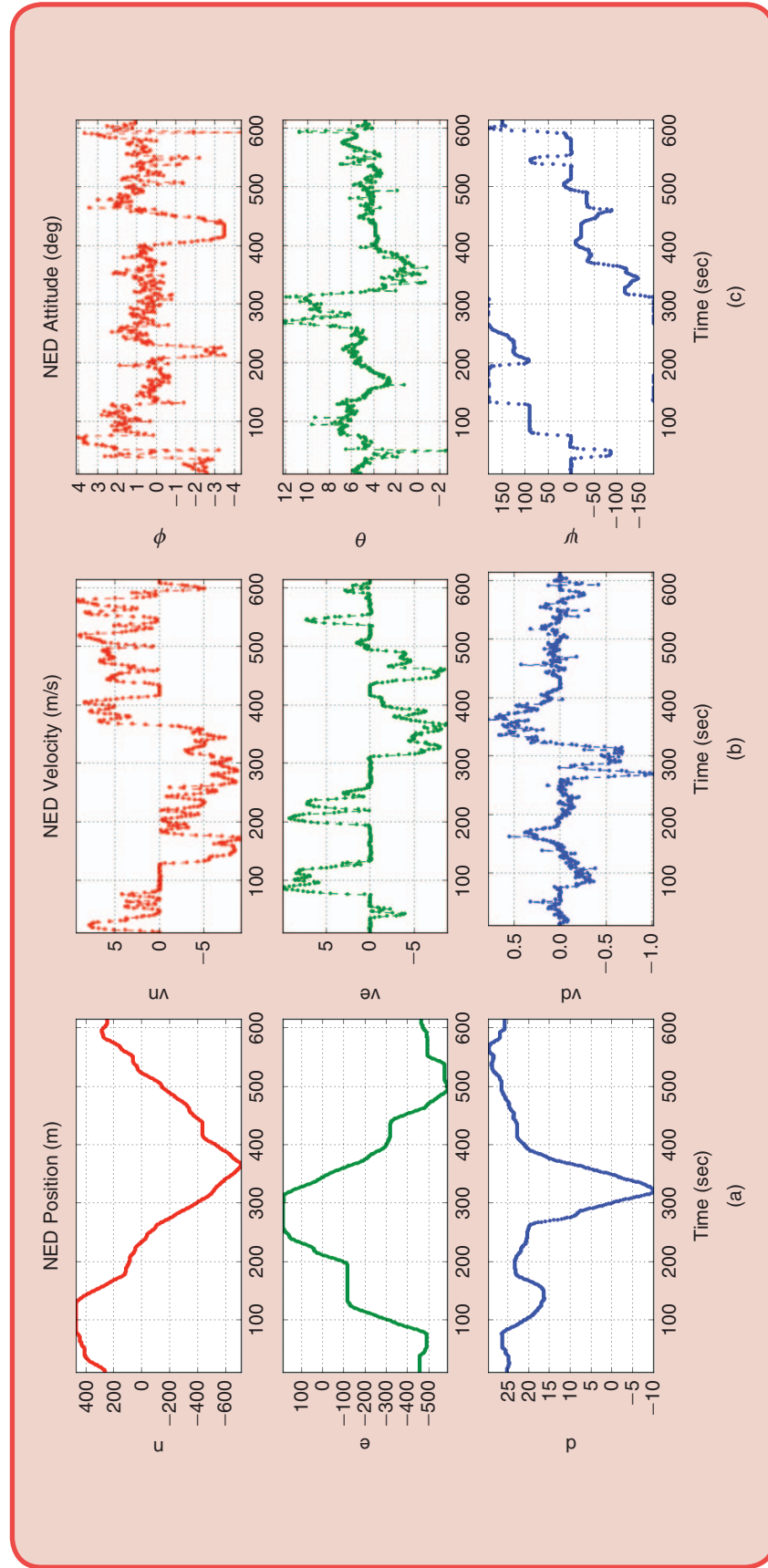


**FIG. 7** Estimated position (a), velocity (b), and attitude (c) represented in NED after going through the entire smoothing process. The attitude plots represent roll (first row), pitch (second row), and yaw (third row) respectively in degrees.

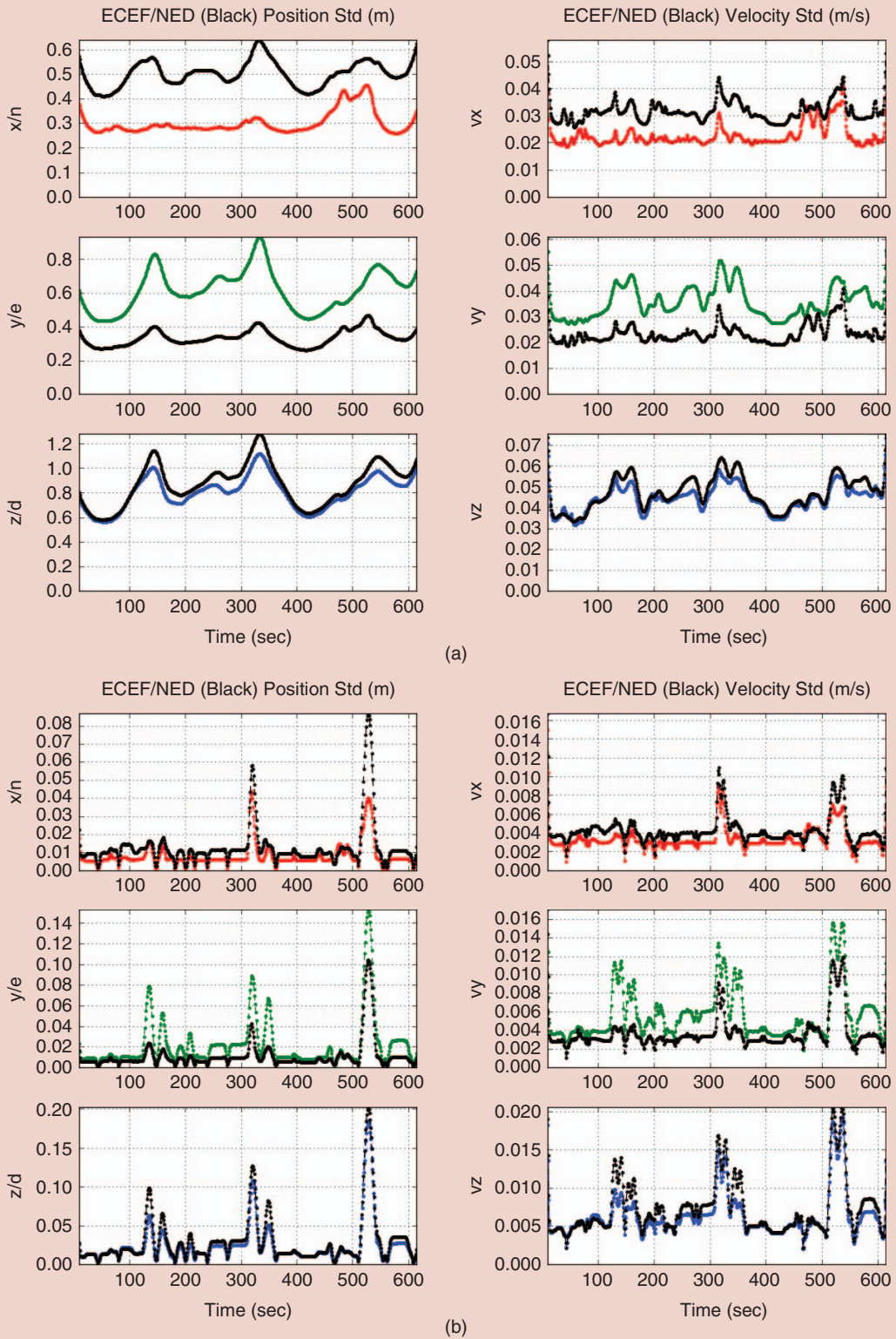


**FIG 8** Plots of the sequence of trajectory error standard deviation estimates computed using eqn. (19). The graphs in (a) are the position and velocity standard deviation plots after the first smoothing stage using only the pseudo-range and Doppler measurements. The graphs in (b) are the position and velocity standard deviation plots after the second smoothing stage using integer-resolved carrier-phase measurements when the integers are available and pseudo-range and Doppler measurements where integers are not available. The red, green, and blue plots represent the uncertainty in ECEF and the black plots represent the uncertainty transformed into NED.

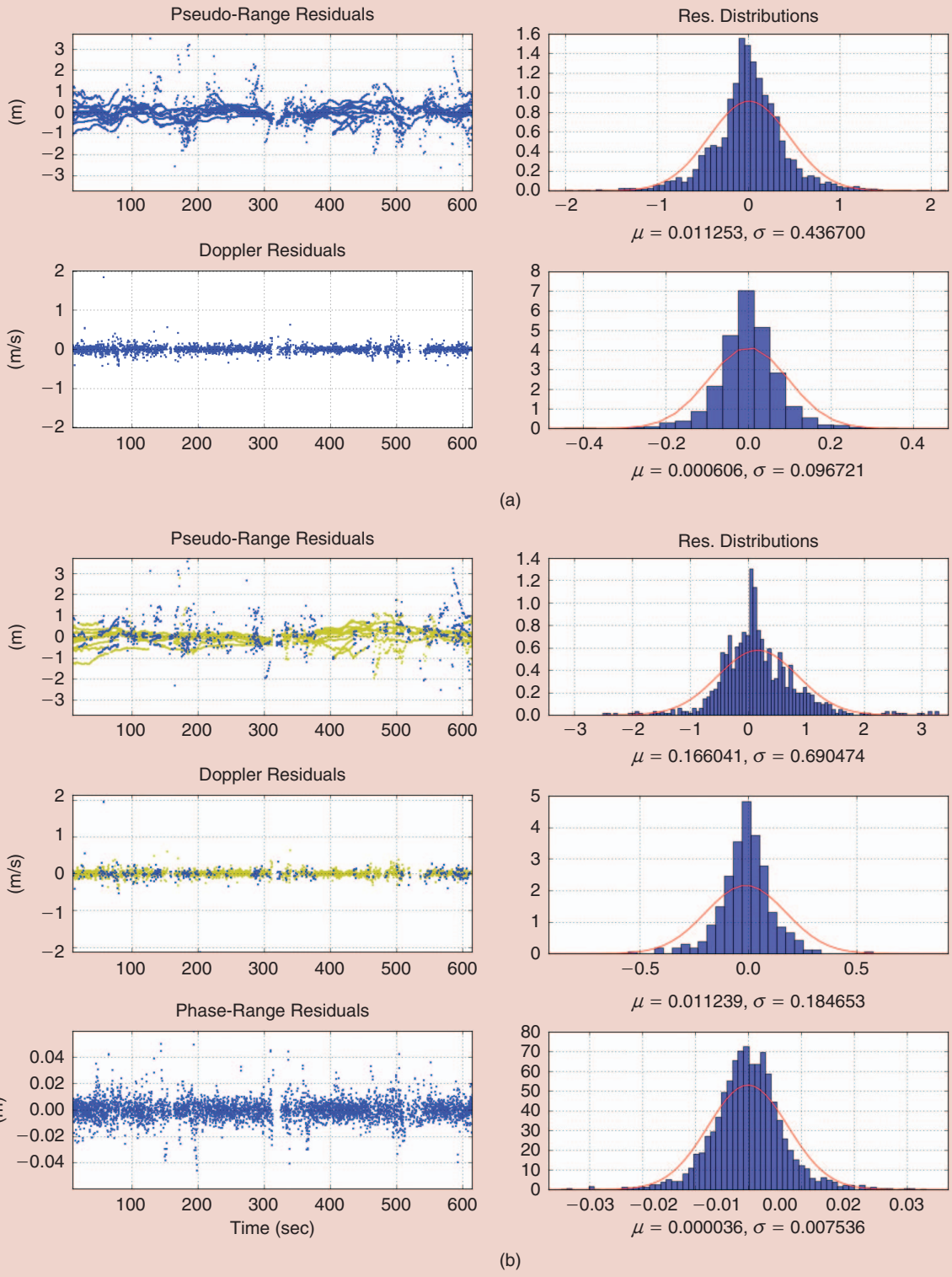


**FIG 9** Plots of the residual sequences  $r(x_{1:M}(t))$  from the final iterations of the first [fig. 8(a)] and second [fig. 8(b)] smoothing stages are shown in the first column (yellow measurement residuals are not utilized in the trajectory estimation). The second column shows the histogram of the residuals utilized in the optimization along with the normalized gaussian approximation plotted in red (the area under the curve integrates to one). (a) Residuals from the final iteration of the smoothing using only pseudo-range and Doppler. (b) Residuals from the final iteration of the smoothing using carrier-phase when integers have been resolved and pseudo-range and Doppler at the remaining epochs.

residuals plotted in yellow are not used in the estimation process and they are not included in the residual histograms. Nevertheless, they are helpful in assessing the performance of the resolved integers used in carrier-phase measurements. The red Gaussian curves in Fig. 9(b) show the normalized (unit area) Gaussian drawn using the mean and standard deviation of the data. These graphs allow us to analyze and quantify the performance of the smoothing process. After the first smoothing stage, the pseudo-range residuals [first row of Fig. 9(a)] have a 0.44 meter standard deviation. At the end of the second smoothing stage, the histogram of the integer-resolved carrier-phase range measurement residuals [third row of Fig. 9(b)] converge to an approximately Gaussian pdf, and the residuals have a standard deviation of 7.5 millimeters. The cost function used to compute Fig. 9(a) utilizes all of the available pseudo-range/Doppler measurements and the cost function used to compute Fig. 9(b) utilizes carrier-phased with resolved integer and pseudo-range/Doppler measurements when carrier-phase is not available; therefore, Figs. 9(a) and 9(b) are distinct. The increase in the pseudo-range and Doppler residual standard deviations seen in Fig. 9(b) when compared to Fig. 9(a) is due to the carrier-phase measurement noise being much smaller, thus, carrier-phase measurements have much higher relative weight compared to pseudo-range and Doppler measurements. In addition, the computed pseudo-range residuals that are not used (drawn in yellow), when carrier-phase is available, generally accounts for the pseudo-range multipath and measurement errors and are within reasonable ranges. The combinations of these quantities indicate that the computed integers are reliable for the trajectory estimation.

## VI. Conclusions and Future Work

This paper presents a method to estimate a sensor platform trajectory with position accurate to the centimeter-level. For navigation and ITS applications, such trajectories can be used as the ground truth to compare localization, SLAM, and visual odometry algorithms. For precision mapping, sensor platform trajectories with this accuracy greatly facilitate the feature detection, association, and tracking subtasks. These are also a necessary requirement for the production of lane-level accuracy ECEF roadway maps. The core contribution of this article is the resolution of the carrier-phase integer ambiguities accurately and reliably, by using multiple epochs of data, and spanning across long time intervals. The entire trajectory is first smoothed using pseudo-range and Doppler measurements. The result is decomposed into smaller segments over which the carrier-phase integer ambiguities can be solved separately. The integers over time segments that pass the validation tests are backward/forward extended, while the locks are maintained, to adjacent intervals which do not have carrier-phase integers

computed. This increases the chances of computing the carrier-phase integers in scenarios where the multipath errors have a significant effect on the measurements.

Future work includes extending this method for mobile roadway mapping where the state information obtained from the method described in this paper can be used in conjunction with feature based sensors (e.g. camera(s), RADAR(s), and LIDAR(s)) to obtain accurate information about the roadway and be able to extract as much information and context from the roadway as possible. Herein we have not used wheel encoder data due to the challenges of receiving high rate, low latency, per wheel encoder data through the CAN bus. Inclusion of encoder data is a potentially beneficial area for future work.

## Acknowledgment

The authors gratefully acknowledge the helpful discussions and technical support provided by Anning Chen, Arvind Ramanandan, Sheng Zhao, and Haiyu Zhang for support throughout idea development, data acquisition and software development.

## About the Authors



**Anh Vu** (S'05) received B.S. degrees (2006) in computer science and electrical engineering, M.S. (2009) and Ph.D. (2011) degrees in electrical engineering from the University of California-Riverside. He is currently a Postdoctoral Scholar at CE-CERT, University of California, Riverside, CA. In 2008, he was a Visiting Student Researcher at Osaka University, Japan, where he conducted research on omnidirectional vision sensing and navigation. In 2012, he was a Visiting Researcher at AIST, Tsukuba, Japan, where he conducted research on multi-target tracking from camera and LIDAR. His research interests include computer vision, robotics, navigation, and machine learning. He received the UCTC Graduate Fellowship in 2006 and the NSF EAPSI Fellowship in 2008.



**Jay A. Farrell** (M'85–SM'98–F'08) received B.S. degrees (1986) in physics and electrical engineering from Iowa State University, and M.S. (1988) and Ph.D. (1989) degrees in electrical engineering from the University of Notre Dame. He is a Professor and two time

Chair of the Department of Electrical Engineering at the University of California–Riverside. For the IEEE Control Systems Society (CSS) he has served as Vice President Finance, as Vice President of Technical Activities, as General Chair of the 2012 IEEE Conference on Decision and Control; and will be President in 2014. He is a Fellow of

the IEEE, a Fellow of AAAS (2011), a Distinguished Member of the IEEE CSS. At Charles Stark Draper Lab (1989–1994), Dr. Farrell received the Engineering Vice President's Best Technical Publication Award in 1990, and Recognition Awards for Outstanding Performance and Achievement in 1991 and 1993. He is author of over 200 technical publications. He is author of the book *Aided Navigation: GPS with High Rate Sensors* (McGraw-Hill 2008), and co-author of the books *The Global Positioning System and Inertial Navigation* (McGraw-Hill, 1998) and *Adaptive Approximation Based Control: Unifying Neural, Fuzzy and Traditional Adaptive Approximation Approaches* (John Wiley 2006).



**Matthew Barth** (M'90–SM'00) received his B.S. degree (1984) in electrical engineering/computer science from the University of Colorado, and M.S. (1986) and Ph.D. (1990) degrees in electrical and computer engineering from the University of California-Santa Barbara.

As a Visiting Research Scholar at Osaka University (1990–1991), he conducted research in robot perception and navigation. He is currently a Professor with the Department of Electrical Engineering and Director of the Center for Environmental Research and Technology (CERT) at the University of California-Riverside. Within the IEEE Intelligent Transportation System Society, Dr. Barth will be President in 2014–2015, is currently the Vice President of Conferences, an Associated Editor of the *Transactions of ITS*, and he has served as a member of the IEEE ITS Society's Board of Governors, and Program Chair for the ITS society's ITSC-08, ITSC-09, and FISTS 2011 conferences. He is also active in several committees of the Transportation Research Board. His research interests include intelligent transportation systems, transportation/emissions modeling, vehicle activity analysis, electric vehicle technology, robotics, and advanced sensing and control.

## References

- [1] S. Mortensen, "USDOT's demonstration and deployment programs on vehicle assist and automation for bus rapid transit," in *Proc. Intelligent Transportation Systems*, 2009.
- [2] I. Skog and P. Hadel, "In-car positioning and navigation technologies—A survey," *IEEE Trans. Intell. Trans. Syst.*, vol. 10, no. 1, pp. 4–21, 2009.
- [3] "Enhanced digital mapping project final report," United States Depart. Transportation, Washington, D.C., 2004.
- [4] K. Li, H.-S. Tan, J. A. Misener, and J. K. Hedrick, "Digital map as a virtual sensor-dynamic road curve reconstruction for a curve speed assistant," *Veh. Syst. Dyn.*, vol. 46, no. 12, pp. 1141–1158, 2008.
- [5] B. Spear, A. Vandervalk, and D. Snyder, "Roadway geometry and inventory trade study for intellidriveSM applications," Federal Highway Administration, Washington, D.C., Tech. Rep. FHWA-HRT-10-075, 2010.
- [6] S. Zhao and J. A. Farrell, "Optimization-based road curve fitting," in *Proc. 2011 50th IEEE Conf. Decision Control European Control Conf.*, pp. 5293–5298.
- [7] A. Vu, A. Ramanandan, A. Chen, J. A. Farrell, and M. Barth, "Real-time computer vision/DGPS-aided inertial navigation system for lane-level vehicle navigation," *IEEE Trans. Intell. Trans. Syst.*, vol. 15, no. 2, pp. 899–915, June 2012.
- [8] N. Trawny, A. Mourikis, S. Roumeliotis, A. Johnson, and J. Montgomery, "Vision-aided inertial navigation for pin-point landing using observations of mapped landmarks," *J. Field Robot.—Special Issue Space Robot.*, vol. 24, no. 5, pp. 557–578, May 2007.
- [9] L. Bai and Y. Wang, "A sensor fusion framework using multiple particle filters for video-based navigation," *IEEE Trans. Intell. Trans. Syst.*, vol. 11, no. 2, pp. 348–358, June 2010.
- [10] I. Miller and M. Campbell, "Particle filtering for map-aided localization in sparse GPS environment," in *Proc. IEEE Int. Conf. Robotics Automation*, 2008, pp. 1834–1841.
- [11] S. Clark and H. Durrant-Whyte, "Autonomous land vehicle navigation using millimeter wave radar," in *Proc. IEEE Int. Conf. Robotics Automation*, 1998, pp. 3697–3702.
- [12] J. Levinson, M. Montemerlo, and S. Thrun, "Map-based precision vehicle localization in urban environments," *Robot.: Sci. Syst.*, June 2007.
- [13] J. Levinson and S. Thrun, "Robust vehicle localization in urban environments using probabilistic maps," *IEEE Int. Conf. Robotics Automation*, 2010, pp. 4572–4578.
- [14] D. Betaille and R. Toledo-Moreo, "Creating enhanced maps for lane level vehicle navigation," *IEEE Trans. Intell. Trans. Syst.*, vol. 11, no. 4, pp. 786–798, Dec. 2010.
- [15] J. Levinson, J. Askeland, J. Dolson, and S. Thrun, "Traffic light mapping, localization, and state detection for autonomous vehicles," in *Proc. IEEE Int. Conf. Robotics Automation*, 2011, pp. 5784–5791.
- [16] J. Choi, J. Lee, D. Kim, G. Sopranı, P. Cerri, A. Broggi, and K. Yi, "Environment-detection-and-mapping algorithm for autonomous driving in rural or off-road environment," *IEEE Trans. Intell. Trans. Syst.*, vol. 13, no. 2, pp. 974–982, June 2012.
- [17] A. Vu, J. Farrell, and M. Barth, "Robust landmark surveying using an integrated camera, carrier-phase DGPS, and inertial navigation system," in *Proc. IJSG/GSS*, 2011.
- [18] A. Vu, J. A. Farrell, R. Vanisthian, and M. Barth, "Improved vehicle trajectory and state estimation using raw GPS and IMU data smoothing," in *Proc. Workshop Navigation, Perception, Accurate Positioning Mapping for Intelligent Vehicles*, 2012.
- [19] P. Maybeck, *Stochastic Models, Estimation, and Control*. vol. 1, New York: Academic Press, 1979.
- [20] T. M. Adams, N.A. Koncz, and A. P. Vonderohe, "Guidelines for the implementation of multimodal transportation location referencing systems," National Research Council, Transportation Research Board, Washington, D.C., NCHRP Tech. Rep. 460, 2001.
- [21] F. Dellaert and M. Kaess, "Square root SAM: Simultaneous location and mapping via square root information smoothing," *Int. J. Robot. Res.*, vol. 25, no. 12, pp. 1181–1203, Dec. 2006.
- [22] S. Thrun, W. Burgard, and D. Fox, *Probabilistic Robotics*. Cambridge, MA: MIT Press, 2005.
- [23] J. Carlson, "Mapping large, urban environments with GPS-Aided SLAM," Ph.D. dissertation, Carnegie Mellon Univ., Pittsburgh, PA, 2010.
- [24] J. Farrell, *Aided navigation: GPS with High Rate Sensors*. New York: McGraw-Hill, 2008.
- [25] S. Maldonado-Bascon, S. Lafuente-Arroyo, P. Gil-Jimenez, H. Gomez-Moreno, and F. Lopez-Ferreras, "Road-sign detection and recognition based on support vector machines," *IEEE Trans. Intell. Trans. Syst.*, vol. 8, no. 2, pp. 264–278, June 2007.
- [26] J. F. Khan, S. M. A. Bhuiyan, and R. R. Adhami, "Image segmentation and shape analysis for road-sign detection," *IEEE Trans. Intell. Trans. Syst.*, vol. 12, no. 2, pp. 85–96, Mar. 2011.
- [27] Z. Kim, "Robust lane detection and tracking in challenging scenarios," *IEEE Trans. Intell. Trans. Syst.*, vol. 9, no. 1, pp. 16–26, June 2008.
- [28] S. Kammel and B. Pitzer, "Lidar-based lane marker detection and mapping," in *Proc. IEEE Intelligent Vehicle Symp.*, June 2008, pp. 1137–1142.
- [29] X.-W. Chang, X. Xie, and T. Zhou, (2011, Oct.). MILES: MATLAB package for solving mixed integer least squares problems. Version 2.0. [Online]. Available: <http://www.cs.mcgill.ca/~chang/software.php>
- [30] X.-W. Chang, X. Yang, and T. Zhou, "MLAMBDA: A modified LAMBDA method for integer least-squares estimation," *J. Geodesy*, vol. 79, no. 9, pp. 552–565, 2005.
- [31] S. Clark and G. Dissanayake, "Simultaneous localization and map building using millimetre wave radar to extract natural features," in *Proc. IEEE Int. Conf. Robotics Automation*, 1999, vol. 2, pp. 1516–1521.
- [32] K. Kimoto and C. Thorpe, "Map building with radar and motion sensors for automated highway vehicle navigation," in *Proc. 1997 IEEE/RSJ Int. Conf. Intelligent Robots Systems*, vol. 3, pp. 1721–1728.
- [33] I. P. Alonso, D. F. Llorca, M. Gavilan, S. A. Pardo, M. A. Garcia-Garrido, L. Vlasic, and M. A. Sotelo, "Accurate global localization using visual odometry and digital maps on urban environments," *IEEE Trans. Intell. Trans. Syst.*, vol. 13, no. 4, pp. 1535–1545, 2012.
- [34] S. Kennedy, D. Cosandier, and J. Hamilton, "GPS/INS integration in real-time and post-processing with NovAtel's SPAN system," in *Proc. Int. Global Navigation Satellite Systems Society Symp.*, 2007.